RSC Advances

ROYAL SOCIETY OF CHEMISTRY

www.rsc.org/advances

Cite this: DOI: 10.1039/c0xx00000x

www.rsc.org/xxxxxx

ARTICLE TYPE

Phase and Structure Development of Spontaneously Ambient-grown $ZnO{\cdot}xH_2O$ and $TiO_2{\cdot}xH_2O$ Nanostructures towards Oxide Single Crystals

Nai-Hao Yang[†a], Shou-Yi Chang*[†b], Chien-Yen Liu[b], Kai-Chieh Wu[a], Su-Jien Lin*[a] and Jien-Wei Yeh[b]

Received (in XXX, XXX) Xth XXXXXXXXX 20XX, Accepted Xth XXXXXXXXX 20XX
DOI: 10.1039/b000000x

Stress-induced $ZnO{\cdot}xH_2O$and $TiO_2{\cdot}xH_2O$ nanocrystals were spontaneously grown in an ambient atmosphere based on a bond breaking-hydrolysis-reconstruction mechanism, without the use of any precursors. The development of their phase and structure towards ZnO and TiO_2 was *in-situ* and *ex-situ* studied. The formation of unstable near-amorphous belt-like orthorhombic $ZnO{\cdot}1.5H_2O$ nanowires and partially crystalline column-like (pyramid top) monoclinic $TiO_2{\cdot}2.5H_2O$ nanorods was initiated in a high relative humidity of 98%, whereas more stable polycrystalline faceted orthorhombic $ZnO{\cdot}H_2O$ nanowires and bamboo leaf-shaped monoclinic $TiO_2{\cdot}0.4H_2O$ nanoflakes were formed in 70% humidity. Upon receiving energy by *in-situ* exposure to an electron beam or *ex-situ* thermal annealing, the $ZnO{\cdot}xH_2O$ and $TiO_2{\cdot}xH_2O$ transformed into hexagonal (wurtzite) ZnO and orthorhombic (brookite) TiO_2, respectively. Exposure of non-polar TiO_2 to an electron beam or annealing generated a polycrystalline structure. Exposure of polar ZnO to a low-energy electron beam formed aligned subgrains, while high-energy annealing yielded a single-crystalline structure, both with a longitudinal $[10\bar{1}0]$ orientation, via a self-assembly process that involved nanocrystallite agglomeration, subgrain tilting and boundary elimination.

Introduction

Low-dimensional nanostructures of metal oxide semiconductors, such as cheap, non-toxic ZnO and TiO_2 with good piezoelectric and photonic properties as well as remarkable photocatalytic activities, have been considered for use in optoelectronic devices, photocatalysis (pollutant degradations), H_2O splitters and even CO_2 converters among other devices. [1-11]. To synthesize low-dimensional ZnO and TiO_2 nanostructures, expensive, high-temperature vaporous processes [3, 12-13] and, in particular, low-cost, low-temperature aqueous (hydrothermal) methods [3-4, 14-21] have been developed. During the reactions of chemical precursors in aqueous processes [20-25], ZnO and TiO_2 hydrate templates, i.e. $ZnO{\cdot}xH_2O$ (typically $Zn(OH)_2$) and $TiO_2{\cdot}xH_2O$ ($Ti(OH)_4$), are initially formed and ultimately transform into ZnO and TiO_2 nanocrystals by a series of hydrolysis-dehydration processes (dissolution-reprecipitation, crystallization and solid-phase transformation) [23]. In all aqueous synthetic routes, chemical precursors with catalysts, additives or surfactants are required, and the surface chemistry (H_2O adsorption/hydrolysis) of reactants [26-28] as well as the structural development and phase transformations of the reaction products [20-25] play important roles in the aqueous growth of oxide nanostructures.

Based on aqueous synthesis and "mechanochemistry" (the breaking of surface bonds of oxides to form oxy-products) [29], we previously developed a bond breaking-hydrolysis-reconstruction (BHR) mechanism [30] by which ZnO and TiO_2 nanocrystals spontaneously grew from films in an ambient atmosphere at room temperature (RT) without the need of chemical precursors or catalysts. The covalent oxide nanocrystals were formed in regions of highly concentrated tensile stress around the crest edges of scratch tracks [30, 31], whereas the extrusion-induced growth of metal whiskers (such as Sn and Bi with weak metallic bonds and high mobility) occurs in regions of compressive stress [32, 33]. The formation of oxide nanocrystals by simple solid-phase transformations in the BHR process without the use of any precursors is of greater interest than aqueous synthesis. A series of reactions, including the ambient adsorption of water or hydroxyl (OH^-; hydrolysis) onto stress-generated surface defects (bond breaking), the subsequent hydration of the oxide surface (large-volume hydrolysis) and the final dehydration (reconstruction) may be important in the ambient growth of oxide nanocrystals. To comprehensively elucidate the BHR mechanism and to systematically clarify the evolution of the BHR products into single-crystalline oxide nanostructures for potential applications, in this study, stress-induced $ZnO{\cdot}xH_2O$ and $TiO_2{\cdot}xH_2O$ template nanostructures were spontaneously grown in an ambient atmosphere with different humidities. Their structural development and phase transformations to crystalline or even single-crystalline ZnO and TiO_2 are studied using transmission electron microscopes (TEMs) both *in-situ* upon exposure to an electron beam and *ex-situ* after thermal annealing.

Experimental section

Thin ZnO and TiO_2 films with a thickness of several hundred nanometers were deposited on Si or glass substrates by a radio-frequency magnetron sputtering using ZnO and TiO_2 targets, respectively. The films were then scratched using a UMIS nanoindenter (Based Model, CSIRO) with a Berkovich diamond tip and a nanoscratch module. The scratch load was ramped up from 0 to 400 mN over a distance of about 1 mm. The scratched samples were then simply stored in a normal ambient atmosphere with a relative humidity (RH) of 40%, 70% or 98% saturated vapor pressure at room temperature for various durations to allow the spontaneous growth of $ZnO{\cdot}xH_2O$ and $TiO_2{\cdot}xH_2O$ nanocrystals. To investigate the phase transformations and structural evolution of the grown nanocrystals, *in-situ* exposure to an electron beam (during TEM observations) or *ex-situ* thermal annealing at 300-500°C for one hour was conducted on the samples that had been stored in the ambient atmosphere. The surface morphologies of the as-grown and the annealed nanocrystals were observed using a scanning electron microscope (SEM, JEOL JSM-6500F), and the microstructures and lattice structures were examined using high-resolution TEMs (JEOL JEM-2100F and FEI Tecnai F20 (low accelerate voltage of 120 kV)) that were equipped with an energy dispersive spectrometer (EDS). Thin foil specimens with nanocrystal/film interfaces (around nanocrystal roots) and short $TiO_2{\cdot}xH_2O$ nanocrystals (covered by a top Pt protective coating) were prepared using a focus ion beam (FIB, FEI Nova-200) at an ultralow current of 1 nA down to 30 pA to avoid any damages that might be caused by ion bombardment. Specimens of long $ZnO{\cdot}xH_2O$ nanowires were attached to a Cu grid (with a graphite film) using an optical microscope that was equipped with three-axis micromanipulation probes (Olympus, BX51). These specimens were then observed using TEMs.

Results and discussion

Stress-induced spontaneous ambient growth

The SEM images in Figure 1a clearly showed the growth of $TiO_2{\cdot}xH_2O$ nanocrystals around the scratch track on a TiO_2 film after the film was scratched and stored in RH 98% at RT for 50 days. Along the scratch track, the applied stress was critical to the growth of the nanocrystals by the BHR mechanism [30]: (1) at the track front under a small stress, almost no nanocrystals were formed, while at the end of the track under a large stress, many nanocrystals appeared; (2) a threshold stress was required to break Ti–O bonds and initiate the growth of nanocrystals; (3) few nanocrystals were formed in the indented region of the scratch track (under a compressive stress) but many were formed at the crest edges (under a tensile stress [31]), unlike the compressive stress-induced growth of Sn whiskers [32]. As shown in Figure 1b, $ZnO{\cdot}xH_2O$ nanowires also grew around the side edges of the tracks at the end of the tracks on scratched ZnO films under the same conditions for a shorter storage period of 20 days. More, longer $ZnO{\cdot}xH_2O$ nanowires than $TiO_2{\cdot}xH_2O$ nanocrystals were grown because the Zn–O bonds were weaker than Ti–O and more easily broken for defect initiation and water adsorption. Long, tangled belt-like nanowires (non-faceted) with a diameter of about 200 nm and a length of about 10 μm grew in RH 98%, while shorter faceted nanowires (three-fold symmetric) with a diameter of 100-200 nm and a length of several μm were formed in RH 70%.

Figure 2 systematically presents the features, amounts and sizes of $TiO_2{\cdot}xH_2O$ nanocrystals that were formed in different humidities, at various temperatures, in various periods of storage. In RH 98% at RT, more and larger nanocrystals grew as the period of storage increased: at 10 days, a few bean-like nanodots with a size of less than 100 nm had just nucleated; at 30 days, more column-like nanorods with diameters of 100-200 nm and lengths of about 400 nm appeared; at 50 days, many more and larger column-like nanorods had grown, clearly exhibiting a faceted feature and a pyramid-like top, similar to those of typical brookite or rutile TiO_2 nanocrystals [3]. In RH 70%, differently structured nanocrystals were formed: long, flat, bamboo leaf-like nanoflakes similar to those of anatase TiO_2 were formed by surface hydration [34], and had a width of about 200 nm and a length of about 1 μm, possibly because the phase/crystal structure differed from that formed in RH 98%. In a dry atmosphere, with RH 40%, the lack of moisture for hydration resulted in the suppressed growth of small dots with a size below 100 nm. At the roots of all nanocrystals, including $ZnO{\cdot}xH_2O$ and $TiO_2{\cdot}xH_2O$, a film-like hydrate base was observed, clearly revealing the prior adsorption of water and hydration of the oxide film surfaces

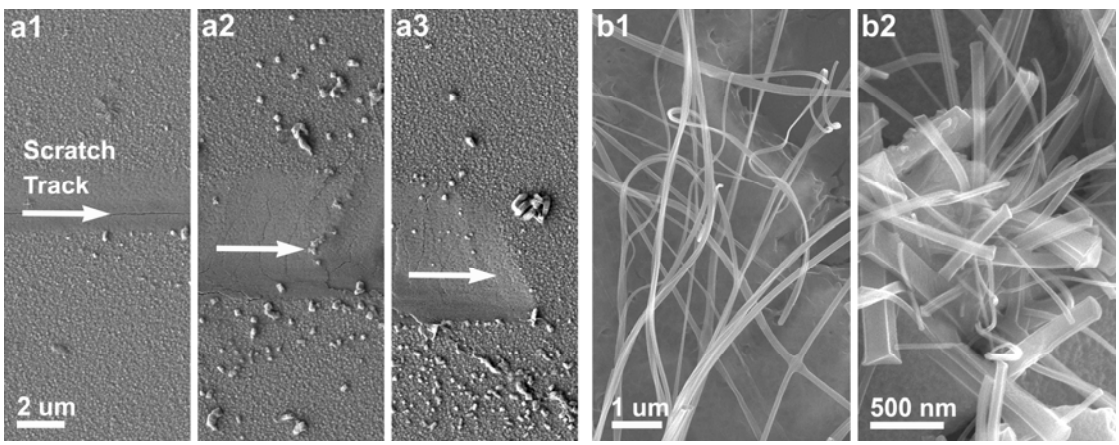

Fig. 1 (a) SEM images of $TiO_2{\cdot}xH_2O$ nanocrystals around a scratch track on a TiO_2 film, formed in RH 98% at RT for 50 days, at the track (a1) front, (a2) center and (a3) end. (b) $ZnO{\cdot}xH_2O$ nanocrystals around scratch tracks on ZnO films, formed in RH (b1) 98% and (b2) 70% at RT for 20 days.

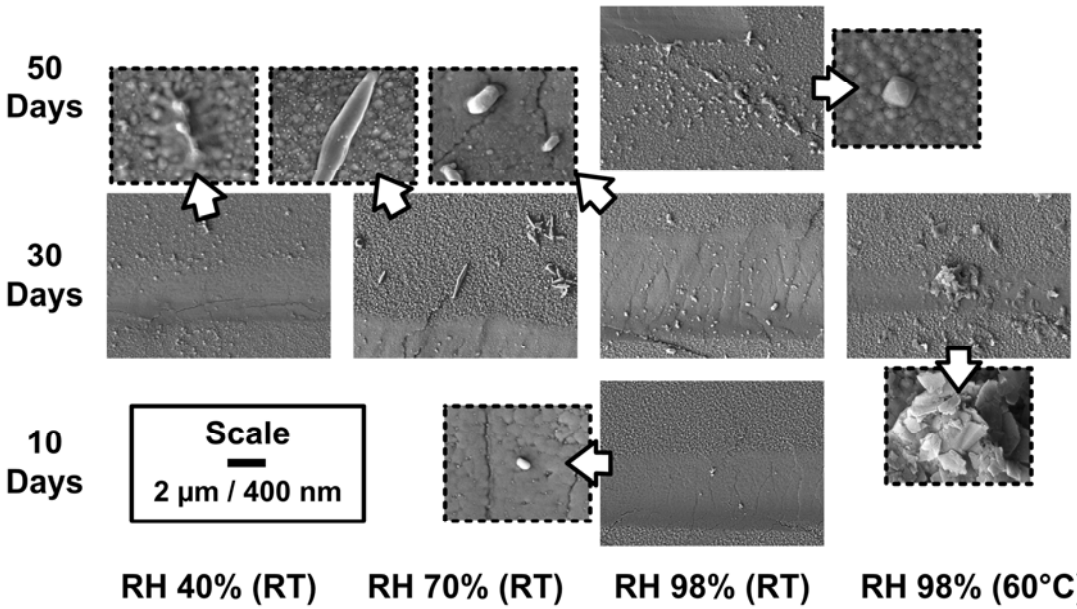

Fig. 2 SEM images of $TiO_2 \cdot xH_2O$ nanocrystals around scratch tracks on TiO_2 films, formed in different humidities, temperatures and durations (scale bar: 2 μm for low-magnification and 400 nm for high-magnification (arrowed and dash line-framed) images).

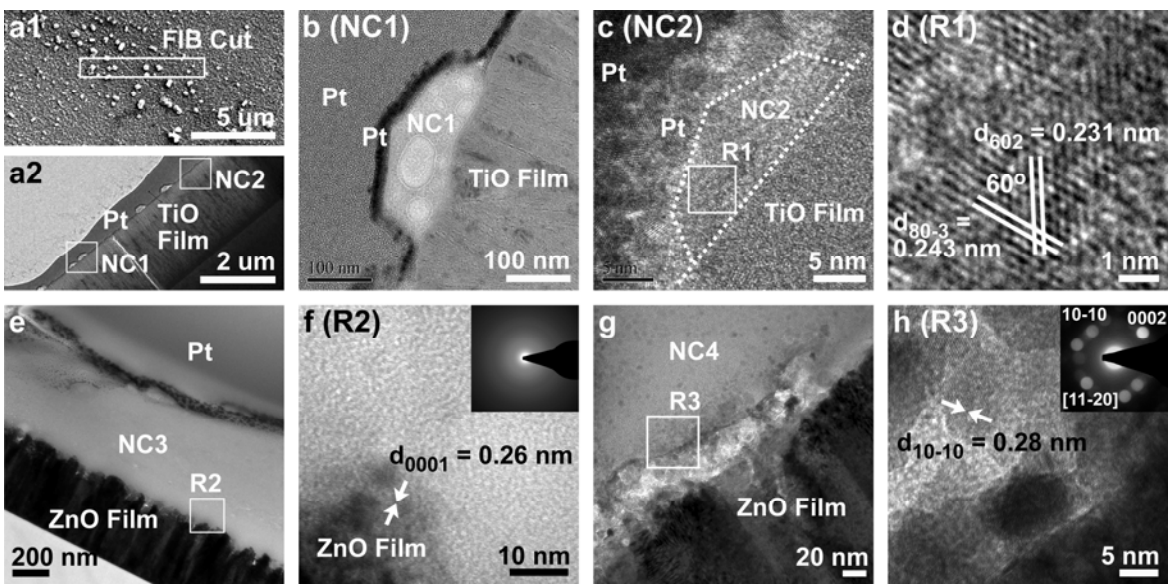

Fig. 3 TEM analyses of $TiO_2 \cdot xH_2O$ nanocrystals around a scratch track on a TiO_2 film, formed in RH 98% at RT for 50 days: (a) specimen preparation by FIB cutting, (b) low-magnification image of nanocrystal 1 (NC1, in a2), (c) high-magnification image of nanocrystal 2 (NC2, in a2), (d) lattice image of region 1 (R1, in NC2 in c). TEM analyses of $ZnO \cdot xH_2O$ nanocrystals around scratch tracks on ZnO films, formed at RT for 20 days: in RH 98%, (e) low-magnification image of nanocrystal 3 (NC3) and (f) high-magnification image of region 2 (R2, in NC3 in e); in RH 70%, (g) low-magnification image of nanocrystal 4 (NC4) and (h) high-magnification image of region 3 (R3, in NC3 in g; insets in f and h: nano-beam SAD patterns).

before the formation of nanocrystals at local stress-caused defects [30]. The sample stored in RH 98% at 60°C however did not exhibit the accelerated longitudinal growth of $TiO_2 \cdot xH_2O$ nanorods, but large stacked nanosheets were formed. At a higher temperature and, consequently, a higher saturated vapor pressure, more moisture and a higher reaction rate induced more and faster hydration, by which the film-like hydrate base on the oxide film surfaces directly and rapidly developed into nanosheets.

Phase and structure initiation in different humidities

Detailed TEM analyses in Figures 3 and 4 reveal the initiation of different structures and phases of $ZnO \cdot xH_2O$ and $TiO_2 \cdot xH_2O$ nanocrystals in different humidities. Notably, during TEM observations, the as-grown hydrate nanocrystals that contained a certain amount of water molecules decomposed (dehydrated) upon exposure to an electron beam, releasing water molecules and causing the gradual formation of bubble-like pores in the nanocrystals or blisters. Therefore, only the structures before decomposition in a very early stage of observation (less than 10 s) were examined. Figures 3a-3c present the short column-like, faceted $TiO_2 \cdot xH_2O$ nanorods (with a pyramid top) that were formed in a high humidity of RH 98%. The high-magnification and lattice images in Figures 3c and 3d revealed a partially crystalline structure that comprised a disordered matrix and some

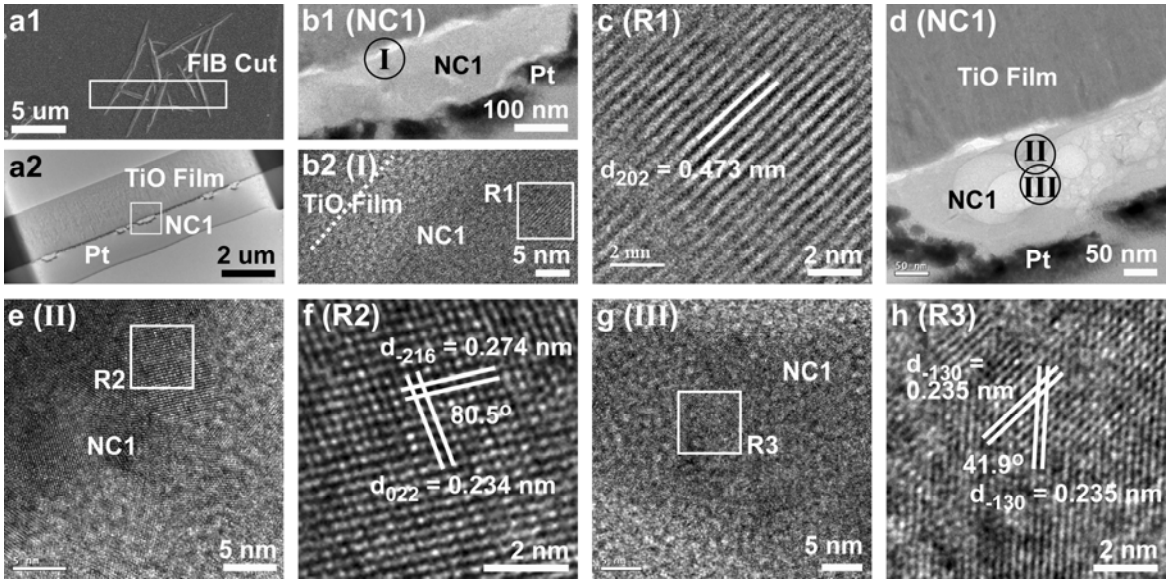

Fig. 4 TEM analyses of $TiO_2{\cdot}xH_2O$ nanocrystals around a scratch track on a TiO_2 film, formed in RH 70% at RT for 50 days: (a) specimen preparation by FIB cutting, (b1) low- and (b2) high-magnification (circle I in b1) images of nanocrystal 1 (NC1, in a2; in an early observation stage), (c) lattice image of region 1 (R1, in circle I in b2); (d) low-magnification image of NC1 (in a2; in a late observation stage), (e) high-magnification image of NC1 (circle II in d; in a late observation stage), (f) lattice image of region 2 (R2, in circle II in e), (g) high-magnification image of NC1 (circled III in d; in a late observation stage), (h) lattice image of region 3 (R3, in circle III in g).

short-range ordered clusters with sizes of several nanometers and with interplanar spacings of $(80\bar{3})$ 0.243 nm and (602) 0.231 nm (angle of 60°), consistent with the structure of monoclinic $Ti_4H_2O_9{\cdot}9H_2O$ (i.e. $TiO_2{\cdot}2.5H_2O$, JCPDS #39-0040). Similarly, as presented in the TEM image and the diffused nano beam SAD pattern in Figures 3e and 3f, the $ZnO{\cdot}xH_2O$, in the form of long belt-like (non-faceted) nanowires, also had an amorphous structure with a Zn:O ratio of 1:2.5 (EDS analyses), suggesting the possible formation of orthorhombic $Zn(OH)_2{\cdot}0.5H_2O$ ($ZnO{\cdot}1.5H_2O$, JCPDS #20-1436). Supplied with abundant moisture for continuous hydration rather than simultaneous dehydration, ZnO and TiO_2 film surfaces in which bonds were broken by stress, particularly around some high-energy column boundaries, were steadily hydrolyzed to form a large amount of hydrates, as revealed by the roughened (down-penetrating) crystal/ film interfaces and the dissolved column boundaries in Figures 3b and 3e. With the hydrates as nuclei and supplements, the protruding $ZnO{\cdot}1.5H_2O$ and $TiO_2{\cdot}2.5H_2O$ nanostructures were formed with a high water content and near-amorphous (partially crystalline, with short-range order) structures.

In lower humidity, RH 70%, less water was incorporated into the formed $ZnO{\cdot}xH_2O$ and $TiO_2{\cdot}xH_2O$ nanocrystals. On the ZnO film surface, as shown in the TEM images in Figures 3g and 3h, polycrystalline $ZnO{\cdot}xH_2O$ nanowires (faceted, three-fold symmetric, as shown in Figure 1b) grew from a film-like hydrate base, and nanograins with sizes of several nanometers (clusters with sizes of several times the lattice parameter) were dispersed in the nanowires. A Zn:O ratio of about 1:2 in some regions and 1:1 in others, the lattice structure with an interplanar spacing of 0.28 nm (ZnO $(10\bar{1}0)$), and the nano-beam SAD spots (ZnO (0002) and $(10\bar{1}0)$, zone axis $[11\bar{2}0]$ [5, 34-35]) in Figure 3h all revealed the formation of crystalline orthorhombic (wulfingite) ε-$Zn(OH)_2$ ($ZnO{\cdot}H_2O$, JCPDS #38-0385) and partly hexagonal (wurtzite) ZnO (JCPDS #36-1451) under concurrent hydration/dehydration in an unsaturated moist atmosphere. Additionally, the TEM analyses in Figures 4a-4c indicated the growth of $TiO_2{\cdot}xH_2O$ nanocrystals with a lower water content in RH 70%: the formed nanoflakes were more stable and so did not decompose until after a long period of exposure to an electron beam (5 min). In the early stage of observation, as presented in Figure 4c, the clear lattice structure with a (202) interplanar spacing of 0.473 nm suggested the formation of partly dehydrated, polycrystalline monoclinic $H_2Ti_5O_{11}{\cdot}H_2O$ ($TiO_2{\cdot}0.4H_2O$, JCPDS #44-0130) in the lower humidity.

The surface chemistry of the ZnO and TiO_2 films, including the adsorption of water or hydroxyl (OH^-) and dehydration, is believed to dominate the above initiation of different-phase $ZnO{\cdot}xH_2O$ and $TiO_2{\cdot}xH_2O$ in different humidities. A range of water adsorption behaviors are proposed based on dynamic density functional calculations and scanning tunneling microscopic analyses of hydrolysis/dehydration in aqueous solutions [34-45]. In this study, tensile stresses facilitate the breakage of Zn–O and Ti–O bonds to form oxygen vacancies, greatly increasing the surface reactivity (or wettability) for water adsorption [36, 37]. The first-layer chemical adsorption of OH^- and H^+ (dissociated from H_2O) onto oxygen vacancies (adsorption energy ~ 0.2 eV, which is much smaller than the adsorption energy of H_2O molecules, ~ 0.7 eV [1, 38-41]) and onto oxygen (to form OH pairs), respectively, forms a monolayer [42] and facilitates the second-layer physical adsorption of H_2O molecules [1, 38-41]. In ZnO as an example, Zn^{+2} at the surface (similar to $Zn^{+2}_{(aq)}$ in aqueous solutions) spontaneously adsorbs OH^-, following reactions (1) and (2) [43]:

$$Zn^{+2}_{(aq)} + OH^- \rightarrow Zn(OH)^+_{(aq)} \quad (\Delta G = -37.58\ \text{kJ/mol}) \qquad (1)$$

$$Zn(OH)^+_{(aq)} + OH^- \rightarrow \varepsilon\text{-}Zn(OH)_{2(cr)} \quad (\Delta G = -58.78\ \text{kJ/mol}) \text{ or (2)}$$

$$Zn(OH)^+_{(aq)} + 2OH^- \rightarrow Zn(OH)^-_{3(aq)} \quad (\Delta G = -50.19\ \text{kJ/mol})$$

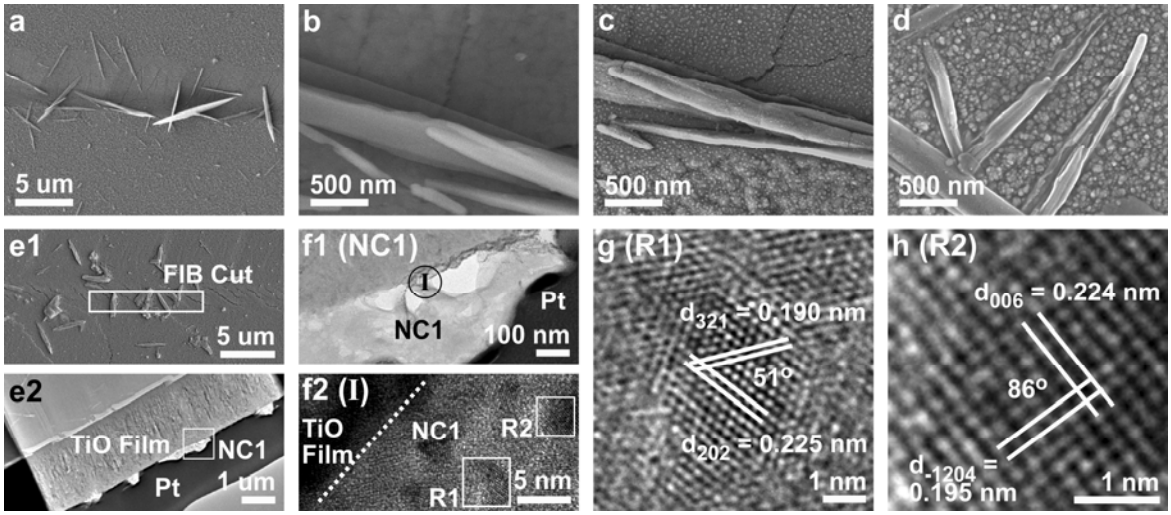

Fig. 5 Nanoscopic structure analyses of annealed $TiO_2{\cdot}xH_2O$ nanocrystals (formed in RH 70% at RT for 180 days). SEM images: as grown, (a) low- and (b) high-magnification images; annealed at (c) 300 and (d) 500°C. TEM analyses, 500°C annealed: (e) specimen preparation by FIB cutting, (f1) low- and (f2) high-magnification (circle I in f1) images of nanocrystal 1 (NC1, in e2; in a late observation stage); lattice images of (g) region 1 (R1) and (h) region 2 (R2, in circle I in f2).

As well, the unstable TiO^{+2} on TiO_2 adsorbs water, possibly as described in reaction (3) [44, 45]:

$$TiO^{+2}_{(s)} + O^{-2} + 2H_2O \rightarrow Ti(OH)_{4(s)} \quad (\Delta H = -675.54\ \text{kJ/mol}) \qquad (3)$$

Similar to the transformation of LiF crystals to LiOH in a humid atmosphere via surface OH^- adsorption and penetrating (inward) hydrolysis [46], ZnO and TiO_2 film surfaces are expected to hydrolyze, forming a hydrate base and protruding hydrate nanostructures. Consistent with the growth of TiO_2 nanocrystals with different phases and morphologies (such as brookite nanorods and anatase nanoflowers) in aqueous synthetic solutions with different OH^- concentrations [47], orthorhombic $ZnO{\cdot}1.5H_2O$ and monoclinic $TiO_2{\cdot}2.5H_2O$, containing a large amount of water, grew in a humid atmosphere, whereas orthorhombic $ZnO{\cdot}H_2O$ or hexagonal (wurtzite) ZnO and monoclinic $TiO_2{\cdot}0.4H_2O$, containing less water were formed at the lower humidity.

***In-situ* and *ex-situ* evolutions of phase and structure**

In the late stage of observation after long-term exposure (5 min) to an electron beam, as presented in Figure 4d, some of the bamboo leaf-like $TiO_2{\cdot}0.4H_2O$ nanocrystals decomposed, and some pores formed in the nanocrystals and the hydrate base. The lattice images of non-decomposed regions in Figures 4e-4h presented several nanocrystallites with interplanar spacings of $(\bar{2}16)$ 0.274 nm and (022) 0.234 nm (angle of 80.5°), $(\bar{2}16)$ 0.274 nm and $(\bar{1}27)$ 0.240 nm (angle of 55°; not presented herein), and (022) 0.235 nm (angle of 41.9°), all corresponding to triclinic Ti_9O_{17} (JCPDS #71-0631). Figures 5a-5d reveals that $TiO_2{\cdot}0.4H_2O$ nanocrystals were more stable under thermal annealing at 300°C but they partially decomposed at 500°C (which is approximately the decomposition temperature of TiO_2 hydrates [48]). In the TEM images of the $TiO_2{\cdot}0.4H_2O$ nanocrystals that were decomposed at 500°C in Figures 5e-5h, most regions were found to have been completely transformed (dehydrate) into polycrystalline TiO_2 with interplanar spacings of (321) 0.190 nm and (202) 0.225 nm (angle of 51°), corresponding to typical orthorhombic (brookite) TiO_2 (JCPDS #76-1934), although very little monoclinic $TiO_2{\cdot}0.4H_2O$ with interplanar spacings of (006) 0.224 nm and $(\bar{1}204)$ 0.195 nm (angle of 86°) remained in Figure 5h (JCPDS #44-0130). The above observations conclude that partially crystalline (short-range-ordered) monoclinic $TiO_2{\cdot}2.5H_2O$ that had formed in high humidity would transform into polycrystalline monoclinic $TiO_2{\cdot}0.4H_2O$ and further into polycrystalline triclinic Ti_9O_{17} or orthorombic (brookite) TiO_2 upon exposure to an electron beam or thermal annealing, similar to reaction (4) [44, 45]:

$$Ti(OH)_{4(s)} \rightarrow TiO_{2(s)} + 2H_2O \quad (\Delta G = -44.9\ \text{kJ/mol}) \qquad (4)$$

The *in-situ* nanoscopic structural analyses, based on the TEM images in Figure 6, captured following exposure to an electron beam, and *ex-situ* observations after annealing at 450°C, shown in Figure 7, suggested the same transformation sequence from near-amorphous $ZnO{\cdot}1.5H_2O$ to crystalline or even single-crystalline ZnO nanowires, when the nanowires received energy. Upon exposure to an electron beam for a very short time (less than 10 s), as verified by the high-resolution TEM images, the nano-beam SAD and fast Fourier transformed (FFT) patterns in Figures 6a and 6d, the $ZnO{\cdot}1.5H_2O$ nanowire had a disordered structure in most regions, yielding diffused hollow diffraction rings, with a few nanoscaled atom clusters (quasi-crystals) with a size of several times the lattice parameter dispersed in the amorphous matrix. As the exposure time was increased (to 1 min), as shown in Figures 6 b and 6e, the nanowire received more energy and began to dehydrate at its surface where the nanocrystallites nucleated and agglomerated forming a clear lattice structure with a size of about 2-3 nm, possibly following reaction (5) [43], in a manner similar to the recovery of LiOH to LiF in a dry atmosphere [46]:

$$\varepsilon\text{-}Zn(OH)_{2(cr)} \rightarrow ZnO_{(cr)} + H_2O \quad (\Delta G = -4.07\ \text{kJ/mol}) \text{ or}$$
$$Zn(OH)^-_{3(aq)} - OH^- \rightarrow ZnO_{(cr)} + H_2O \quad (\Delta G = -16.73\ \text{kJ/mol}) \qquad (5)$$

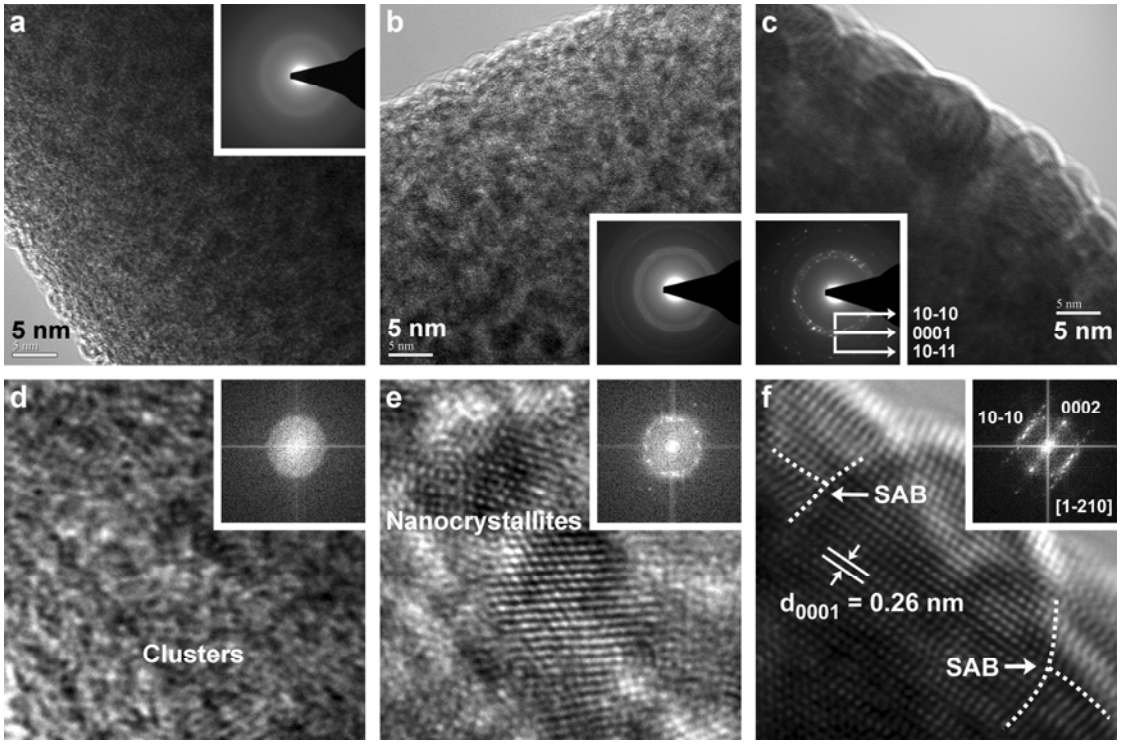

Fig. 6 *In-situ* nanoscopic structure analyses of ZnO·xH$_2$O nanowires (formed in RH 98% at RT for 20 days) under an electron beam exposure. High-resolution TEM images: exposed for (a) less than 10 sec, (b) 1 min, (c) 5 min (insets: nano-beam SAD patterns); lattice images: exposed for (a) less than 10 sec, (b) 1 min, (c) 5 min (ZnO wurtzite structure, SAB: small-angle subgrain boundary; insets: FFT patterns along a $[1\bar{2}10]$ axis)

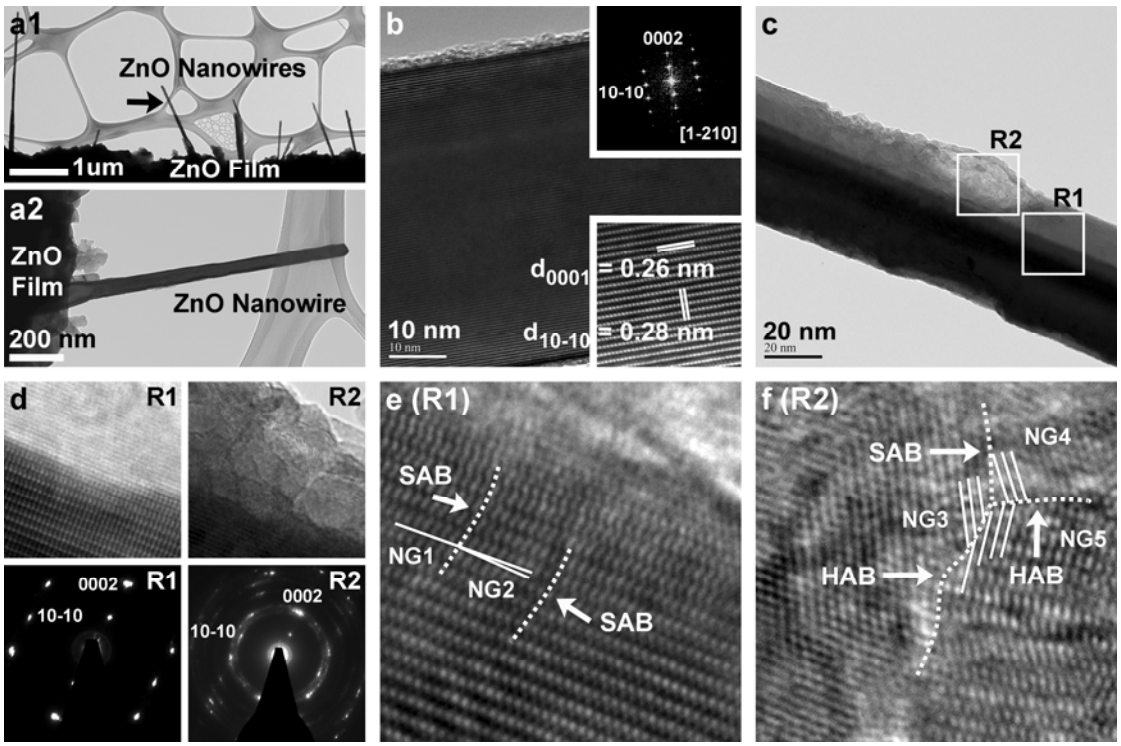

Fig. 7 Nanoscopic structure analyses of 450°C annealed ZnO·xH$_2$O nanowires (formed in RH 98% at RT for 20 days). TEM analyses of single-crystalline ZnO nanowire: (a1) low- and (a2) high-magnification images (background: graphite film on a Cu grid), (b) high-resolution image (insets: FFT pattern along a $[1\bar{2}10]$ axis and lattice image). TEM analyses of single-crystalline ZnO nanowire with a polycrystalline defect: (c) high-magnification image, (d) high-resolution images and nano-beam SAD patterns of region1 (R1) and region 2 (R2, in c); lattice images of (e) R1 and (f) R2 (in d; SAB: small-angle subgrain boundary, HAB: high-angle subgrain boundary; dashed lines: subgrain boundaries; solid lines: lattice orientations of small-angle subgrains NG1 and NG2 in e and high-angle subgrains NG3, NG4 and NG5 in f).

As verified by the lattice images and the nano beam SAD and FFT patterns in Figures 6c and 6f, polycrystalline hexagonal (wurtzite) ZnO with a (0001) interplanar spacing of 0.26 nm was ultimately formed, and crystallization and grain growth to 5-10 nm via nanocrystallite agglomeration were observed after long-term exposure (5 min) to an electron beam. The nanocrystallites (or subgrains) tilted with a longitudinal $[\,10\bar{1}0\,]$ preferred orientation, leaving {0001} surfaces and the small-angle subgrain boundaries (SABs) among the aligned nanocrystallites. When the exposure was extended further (10 min), the subgrain structure remained due to the inefficiency of a low-energy electron beam in eliminating SABs.

The high energy provided by thermal annealing activated much complete dehydration and structural evolution of $ZnO{\cdot}1.5H_2O$ to ZnO. As observed in Figures 7a and 7b, annealing at 450°C geberated a perfect lattice structure with a (0001) interplanar spacing of 0.26 nm and a $(10\bar{1}0)$ spacing of 0.28 nm, as well as simple FFT diffraction spots and a stoichiometric Zn:O ratio of 1:1, indicating further subgrain tilting and boundary elimination, which yielded the longitudinal $[\,10\bar{1}0\,]$ orientation and (0001) surface of single-crystalline hexagonal (wurtzite) ZnO nanowires. However, probably due to non-uniform dehydration, a few bump-like or blister defects with a polycrystalline structure were also observed on the surfaces of some single-crystalline nanowires, as presented in Figures 7c and 7d. The lattice images that were obtained around a defect, shown in Figures 7e and 7f, in which different lattice orientations of several small- and high-angle subgrains are marked, clearly reveal the presence of SABs in the near-single-crystalline region and high-angle boundaries (HABs) in the polycrystalline region. Figure 8 schematically depicts the structural development of amorphous $ZnO{\cdot}1.5H_2O$ to single-crystalline ZnO nanowire (without or with a polycrystalline defect). From Figure 8a, soon after an amorphous $ZnO{\cdot}1.5H_2O$ nanowire receives energy, dehydration occurs firstly on both surfaces where ZnO clusters begin to precipitate. More nanocrystallites then form and grow preferentially along the [0001] direction (inwards) into columnar subgrains that have SABs and {0001} surfaces. A self-assembly process that includes nanocrystallite agglomeration, subgrain tilting and boundary elimination ultimately yields a single-crystalline ZnO nanowire. Three main growth directions ([0001], $[10\bar{1}0]$ and $[1\bar{2}10]$) of wurtzite ZnO structure, dependent on the experimental parameters and morphology, have been reported [49]. In this study, the observed longitudinal $[10\bar{1}0]$ growth of the nanowires, with {0001} top/bottom surfaces and $(1\bar{2}10)$ side surfaces, is attributable to polar surface-induced growth to reduce electrostatic energy, as proposed by Korgel and Kong [50, 51]: when ZnO nanocrystallites form on surfaces, the Zn-terminated (0001) surface is positively charged, and the O-terminated $(000\bar{1})$ surface is negatively charged; agglomerated nanocrystallites with surface polar charges are then automatically rearranged in parallel to reduce total electrostatic energy, causing small-angle alignment (with $(0001)/(000\bar{1})$ surfaces perpendicular to longitudinal $[\,10\bar{1}0\,]$). However, in Figure 8b, non-uniform dehydration, such as by the early heating of the $ZnO{\cdot}1.5H_2O$ nanowire interior, causes the aggregation and expansion of released water molecules below surface, forming a blister, which interferes with the parallel alignment and packing of polarized ZnO nanocrystallites. High-angle boundaries are therefore left around the blister, generating polycrystalline defects on the surfaces of some single-crystalline nanowires. In contrast, for non-polar TiO_2 without electrostatic energy, a randomly polycrystalline structure is formed either upon exposure to a low-energy electron beam or by high-energy thermal annealing. Similar to the polycrystalline ZnO structure with blister defects and HABs, agglomerated non-polar TiO_2 nanocrystallites of different orientations, also with HABs, barely tilt for boundary elimination even when they receive high energy over a long period, so a polycrystalline TiO_2 structure remains.

The fact that the stress-induced spontaneous growth of $ZnO{\cdot}xH_2O$ and $TiO_2{\cdot}xH_2O$ nanostructures of a certain length (of the order of micrometers) in the ambient atmosphere takes as long as several to tens of days is unpromising. However, this work promotes the development of a new route that facilitates surface hydrolysis for the next formation of hydrate/oxide nanocrystals.Additionally, the *in-situ* and *ex-situ* investigations herein are believed to contribute towards our understanding of the underlying mechanism of the phase and structural transformations of hydrates towards oxides although thermal annealing that accelerates dehydration may change the final phases of ZnO and TiO_2 from those that are slowly formed at room temperature.

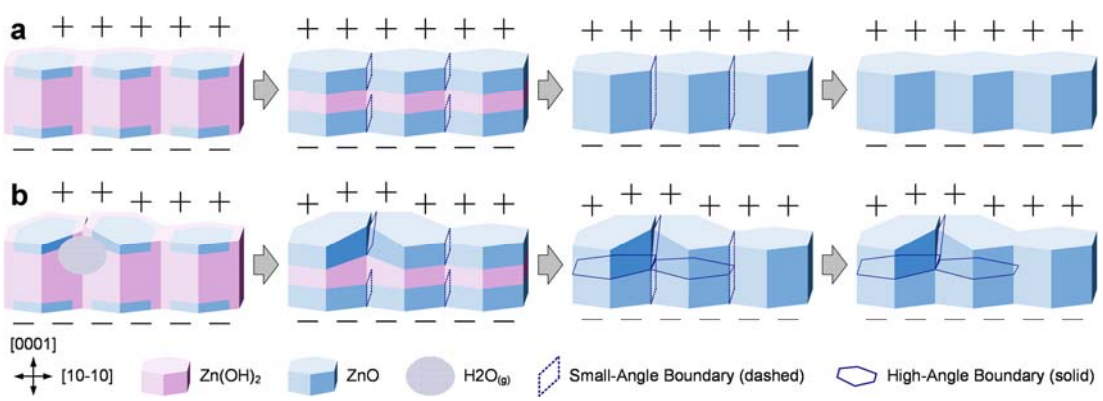

Fig. 8 Schematic illustrations of structure developments of spontaneously ambient-grown amorphous $ZnO{\cdot}xH_2O$ to crystalline ZnO nanowires: (a) a single-crystalline structure, (b) a single-crystalline structure with a polycrystalline defect.

Conclusions

The phase and structural transformations of stress-induced $ZnO{\cdot}xH_2O$ and $TiO_2{\cdot}xH_2O$ nanocrystals that spontaneously grew in an ambient atmosphere with different humidities without the use of any chemical precursors were studied *in-situ* upon exposure to an electron beam and *ex-situ* after thermal annealing to elucidate their development into ZnO and TiO_2. As confirmed by nanoscopic analyses, water adsorption/dehydration-dependent surface chemistry dominated the initiation of $ZnO{\cdot}xH_2O$ and $TiO_2{\cdot}xH_2O$. In a saturated moisture atmosphere, near-amorphous belt-like orthorhombic $ZnO{\cdot}1.5H_2O$ nanowires and partially crystalline column-like monoclinic $TiO_2{\cdot}2.5H_2O$ nanorods were formed; in lower humidity, polycrystalline faceted orthorhombic $ZnO{\cdot}H_2O$ nanowires and bamboo leaf-shaped monoclinic $TiO_2{\cdot}0.4H_2O$ nanoflakes developed. When the $ZnO{\cdot}xH_2O$and $TiO_2{\cdot}xH_2O$ received thermal energy, hexagonal wurtzite ZnO and orthorhombic brookite TiO_2 nanocrystallites nucleated. Polarity induced the formation of single-crystalline ZnO nanowires with a $[10\bar{1}0]$ orientation and {0001} surfaces via self-assembly, which included nanocrystallite agglomeration, subgrain tilting and boundary elimination.

Acknowledgements

The authors gratefully acknowledge the financial supports provided for this research by the National Science Council, Taiwan, under Grant No. NSC-102-2221-E-005-026-MY3, and in part by the Ministry of Education, Taiwan, under the ATU plan. Ted Knoy is appreciated for his editorial assistance.

Notes

[a] *Department of Materials Science and Engineering, National Tsing Hua University, Hsinchu 30013, Taiwan.*
[b] *Department of Materials Science and Engineering, National Chung Hsing University, Taichung 40227, Taiwan.*
** Corresponding Authors. Fax: +886 4 22857017; Tel: +886 4 22857517; e-mail: shouyi@dragon.nchu.edu.tw (S.Y.C.). Fax: +886 3 5722366; Tel: +886 3 5719543; e-mail: sjlin@mx.nthu.edu.tw (S.J.L.).*
† The authors contributed equally.

References

1 U. Diebold, *Surf. Sci. Rep.*, 2003, **48**, 53-229.
2 O. Carp, C. L. Huisman and A. Reller, *Prog. Solid State Ch.*, 2004, **32**, 33-177.
3 X. Chen and S. S. Mao, *Chem. Rev.*, 2007, **107**, 2891-2959.
4 Z. L. Wang, Maert. Sci. Eng. R 2009, **64**, 33-71.
5 Z. L. Wang, R. Yang, J. Zhou, Y. Qin, C. Xu, Y. Hu and S. Xu, *Mater. Sci. Eng. R*, 2010, **70**, 320-329.
6 S. Barth, F. H. Ramirez, J. D. Holmes and A. R. Rodriguez, *Prog. Mater. Sci.*, 2010, **55**, 563-627.
7 S. Xu, Y. Qin, C. Xu, Y. Wei, R. Yang and Z. L. Wang, *Nat. Nanotechnol.*, 2010, **5**, 366-373.
8 K. J. Choi and H. W. Jang, *Sensors*, 2010, **10**, 4083-4099.
9 Y. C. Huang, S. Y. Chang, C. F. Lin and W. J. Tseng, *J. Mater. Chem.*, 2011, **21**, 14056-14061.
10 J. Song, Y. Zhang, C. Xu, W. Wu and Z. L. Wang, *Nano Lett.*, 2011, **11**, 2829-2834.
11 S. Chu, G. Wang, W. Zhou, Y. Lin, L. Chernyak, J. Zhao, J. Kong, L. Li, J. Ren and J. Liu, *Nat. Nanotechnol.*, 2011, **6**, 506-510.
12 J. J. Wu and C. C. Yu, *J. Phys. Chem. B*, 2004, **108**, 3377-3379.
13 C. A. Chen, Y. M. Chen, Y. S. Huang, D. S. Tsai, K. K. Tiong and P. C. Liao, *CrystEngComm*, 2009, **11**, 2313-2318.
14 Q. Zhang and L. Gao, *Langmuir*, 2003, **19**, 967-971.
15 Y. Yu and D. Xu, *Appl. Catal. B-Environ.*, 2007, **73**, 166-171.
16 X. Y. Kong and Z. L. Wang, Nano Lett., 2003, **3**, 1625-1631.
17 J. S. Na, B. Gong, G. Scarel and G. N. Parsons, *ACS Nano*, 2009, **3**, 3191-3199.
18 Y. Sun, L. Wang, X. Yu and K. Chen, *CrystEngComm*, 2012, **14**, 3199-3204.
19 R. Shi, P. Yang, J. Wang, A. Zhang, Y. Zhu, Y. Cao and Q. Ma, *CrystEngComm*, 2012, **14**, 5996-6003.
20 N. T. Khoa, S. W. Kim, D. V. Thuan, D. H. Yoo, E. J. Kim and S. H. Hahn, *CrystEngComm*, 2014, **16**, 1344-1350.
21 N. T. Khoa, S. W. Kim, D. H. Yoo, S. Cho, E. J. Kim and S. H. Hahn, *ACS Appl. Mater. Interfaces*, 2015, **7**, 3524-3531.
22 T. Ichikawa and S. Shiratori, *Inorg. Chem.*, 2011, **50**, 999-1004.
23 S. Xu and Z. L. Wang, *Nano Res.*, 2011, **4**, 1013-1098.
24 M. Wang, Y. Zhou, Y. Zhang, S. H. Hahn and E.J. Kim, *CrystEngComm*, 2011, **13**, 6024-6026.
25 N. J. Nicholas, G. V. Franks and W. A. Ducker, *CrystEngComm*, 2012, **14**, 1232-1240.
26 Y. Ding and Z. L. Wang, *Surf. Sci.*, 2007, **601**, 425-433.
27 A. Önsten, D. Stoltz, P. Palmgren, S. Yu, M. Göthelid and U. O. Karlsson, *J. Phys. Chem. C*, 2010, **114**, 11157-11161.
28 J. T. Newberg, D. E. Starr, S. Yamamoto, S. Kaya, T. Kendelewicz, E. R. Mysak, S. Porsgaard, M. B. Salmeron, G. E. Brown, J. A. Nilsson and H. Bluhm, *J. Phys. Chem. C*, 2011, **115**, 12864-12872.
29 S. L. James, C. J. Adams, C. Bolm, D. Braga, P. Collier, T. Friščić, F. Grepioni, K. D. M. Harris, G. Hyett, W. Jones, A. Krebs, J. Mack, L. Maini, A. G. Orpen, I. P. Parkin, W. C. Shearouse, J. W. Steedk and D. C. Waddelli, *Chem. Soc. Rev.*, 2012, **41**, 413-447.
30 S. Y. Chang, N. H. Yang, Y. C. Huang, S. J. Lin, T. Z. Kattamis and C. Y. Liu, *J. Mater. Chem.*, 2011, **21**, 4264-4271.
31 T. Shibutani, Q. Yu, T. Yamashita and M. Shiratori, *IEEE T. Electron. Pack.*, 2006, **29**, 259-264.
32 W. Shim, J. Ham, K. Lee, W. Y. Jeung, M. Johnson and W. Lee, *Nano Lett.*, 2009, **9**, 18-22.
33 M. D. Vaudin, Y. B. Gerbig, S. J. Stranick and R. F. Cook, *Appl. Phys. Lett.*, 2008, **93**, 193116.
34 C. Wöll, Prog. *Surf. Sci.*, 2007, **82**, 55-120.
35 D. Raymand, A. C. T. van Duin, W. A. Goddard III, K. Hermansson and D. Spångberg, *J. Phys. Chem. C*, 2011, **115**, 8573-8579.
36 A. Calzolari and A. Catellani, *J. Phys. Chem. C*, 2009, **113**, 2896-2902.
37 H. Hu, H. F. Ji and Y. Sun, *Phys. Chem. Chem. Phys.*, 2013, **15**, 16557-16565.
38 H. Zhou, H. Alves, D. M. Hofmann, W. Kriegseis, B. K. Meyer, G. Kaczmarczyk and A. Hoffmann, *Appl. Phys. Lett.*, 2002, **80**, 210-212.
39 Y. He, W. K. Li, X. Q. Gong, O. Dulub, A. Selloni and U. Diebold, U. *J. Phys. Chem.*, C 2009, **113**, 10329-10332.
40 X. Cui, Z. Wang, S. Tan, B. Wang, J. Yang and J. G. Hou, *J. Phys. Chem. C*, 2009, **113**, 13204-13208.
41 C. Sun, L. M. Liu, A. Selloni, G. Q. Lu and S. C. Smith, *J. Mater. Chem.*, 2010, **20**, 10319-10334.
42 O. Dulub, B. Meyer and U. Diebold, *Phys. Rev. Lett.*, 2005, **95**, 136101.
43 A. Moezzi, M. Cortie and A. McDonagh, *Dalton Trans.*, 2011, **40**, 4871-4878.
44 K. G. Knauss, M. J. Dibley, W. L. Bourcier and H. F. Shaw, *Appl. Geochem.*, 2001, 16, 1115-1128.
45 V. N. Misra, S. C. Das and T. Subbaiah, *Emerging Trends in Mineral Processing and Extractive Metallurgy*, Allied Publishers, Delhi, India, 2005, p. 497.
46 S. Sakthivel, M. V. Shankar, M. Palanichamy, B. Arabindoo, D. W. Bahnemann and V. Murugesan, *Water Res.*, 2004, **38**, 3001-3008.
47 Y. H. Jin, S. H. Lee, H. W. Shim, K. H. Ko and D. W. Kim, *Electrochim. Acta*, 2010, **55**, 7315-7321.
48 S. Bela, A. S. W. Wong and G. W. Ho, *J. Phys. D: Appl. Phys.*, 2010, **43**, 035401.
49 Z. L. Wang, *J. Phys.: Condens. Matter.*, 2004, **16**, R829-R858.

50 B. A. Korgel, *Science*, 2004, **303**, 1308-1309.

51 X. Y. Kong, Y. Ding, R. Yang and Z. L. Wang, *Science*, 2004, **303**, 1348-1351.